



Enhancing the energy potential of food waste digestate via catalytic co-hydrothermal treatment: The pyrolysis and combustion performance of hydrochar

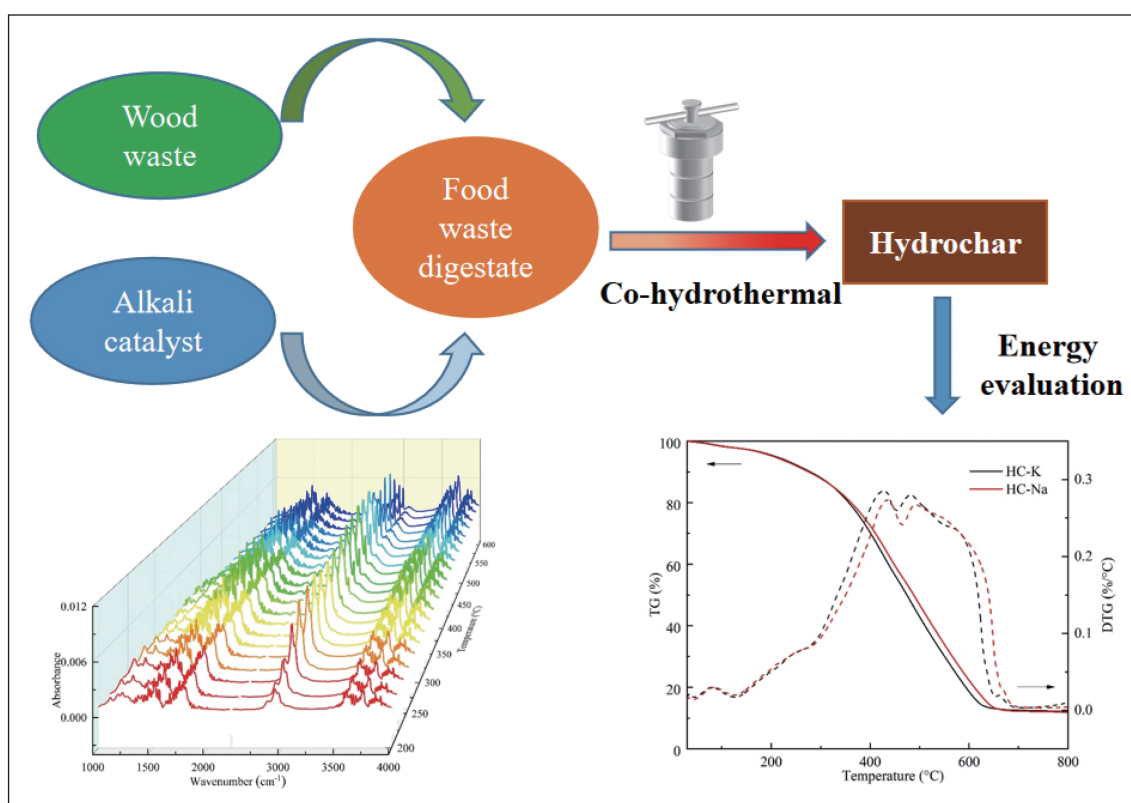
Xiefei Zhu , and Zejun Luo

Department of Thermal Science and Energy Engineering, University of Science and Technology of China, Hefei 230027, China

Correspondence: Xiefei Zhu, E-mail: xiefzhu@ustc.edu.cn

© 2022 The Author(s). This is an open access article under the CC BY-NC-ND 4.0 license (<http://creativecommons.org/licenses/by-nc-nd/4.0/>).

Graphical abstract




Hydrochar derived from food waste digestate through catalytic co-hydrothermal treatment has excellent energy potential.


Public summary

- Carbon-rich hydrochar with a high heating value was prepared from food waste digestate and wood waste via catalytic co-hydrothermal treatment.
- Hydrochar possessed abundant functional groups and retained alkali metal elements.
- Hydrochar demonstrated comprehensive combustion performance and superior combustion reactivity.

Enhancing the energy potential of food waste digestate via catalytic co-hydrothermal treatment: The pyrolysis and combustion performance of hydrochar

Xiefei Zhu , and Zejun Luo

Department of Thermal Science and Energy Engineering, University of Science and Technology of China, Hefei 230027, China

 Correspondence: Xiefei Zhu, E-mail: xiefzhu@ustc.edu.cn

© 2022 The Author(s). This is an open access article under the CC BY-NC-ND 4.0 license (<http://creativecommons.org/licenses/by-nc-nd/4.0/>).



Cite This: *JUSTC*, 2022, 52(7): 3 (8pp)



Read Online



Supporting Information

Abstract: Catalytic hydrothermal treatment is considered one of the most promising technologies for recovering energy from carbonaceous wastes. In so doing, it facilitates the realization of waste-to-energy and resource utilization efforts. In this study, hydrochar was prepared from food waste digestate and wood waste via catalytic co-hydrothermal treatment using potassium carbonate (K_2CO_3) and sodium carbonate (Na_2CO_3) as alkali catalysts. Based on the physicochemical properties of hydrochar, including proximate analysis, element distribution, high heating value (HHV), surface functional groups, and morphology, the gaseous products of pyrolysis and the combustion performance of hydrochar were further investigated using TG-FTIR-MS and TG-DSC, respectively. In addition, the hydrochar combustion kinetics and thermodynamics were probed. Specifically, the hydrochar obtained from Na_2CO_3 catalysis (HC-Na) demonstrated a higher heating value ($26.85 \text{ MJ}\cdot\text{kg}^{-1}$) with higher calcium retention, while the hydrochar obtained from K_2CO_3 catalysis (HC-K) had a greater number of functional groups and larger carbon content. Moreover, the pyrolysis gaseous products of hydrochar were rich in hydrocarbons. HC-K exhibited better comprehensive combustion performance with the activation energy (E_a) values of $79.32 \text{ kJ}\cdot\text{mol}^{-1}$ and $67.91 \text{ kJ}\cdot\text{mol}^{-1}$ using the Flynn-Wall-Ozawa and Kissinger-Akahira-Sunose methods, respectively. These results provide a prospect for enhancing the comprehensive utilization of carbonaceous solid waste through catalytic co-hydrothermal treatment.

Keywords: hydrochar; catalyst; physicochemical properties; gaseous products; kinetics

CLC number: X705

Document code: A

1 Introduction

To achieve carbon peaking and carbon neutrality, the pursuit of clean and sustainable energy has been attracting increasing attention^[1-3]. Energy recovery from carbonaceous wastes such as biomass^[4], animal manure^[5], and food waste^[6] is a promising pathway that not only provides energy, but also contributes to waste treatment, thereby multiplying the environmental benefits. Food waste digestate, the residue of the anaerobic digestion of food waste, is usually used for soil improvement, but this inevitably brings about new environmental problems, such as odor, pathogen exposure, and greenhouse gas production^[7,8]. Therefore, to avoid the environmental issues caused by dealing with food waste digestate, and to further exploit its energy potential, hydrothermal treatment is considered a promising energy conversion method to realize the energy utilization of food waste digestate^[9]. Zhang et al.^[10] explored the dehydration mechanism of food waste digestate during hydrothermal treatment. When the temperature of hydrothermal treatment was above $180 \text{ }^\circ\text{C}$, the bound water was removed through the polymerization and aromatization reactions. Xie et al.^[11] studied the pyrolysis kinetics of hydrochar

obtained from the microwave-assisted hydrothermal carbonization of food waste digestate, and found that the activation energy (E_a) value of hydrochar was in the range of $85.2\text{--}106.5 \text{ kJ}\cdot\text{mol}^{-1}$. Zhang et al.^[12] evaluated the management and valorization of food waste digestate through a hydrothermal process, and found that metal elements tended to aggregate into solid products, whereas carbon was mostly dissolved in liquids.

Unlike the hydrothermal treatment of biomass, food waste digestate contains a high ash content (generally greater than 30%), which limits the product yield and quality of the direct hydrothermal process^[13]. The addition of low-ash biomass to the hydrothermal system is an excellent strategy for improving product yield and quality^[14,15]. Lang et al.^[16] explored the effects of adding corn stalk to swine manure during the hydrothermal process, and found that the addition of corn stalk significantly enhanced the combustion performance of hydrochar. Lu et al.^[17] studied the addition of lignocellulosic biomass to sewage sludge in co-hydrothermal carbonization, and found that the presence of biomass can optimize the transfer of heavy metals and increase the heating value of hydrochar. Sharma et al.^[18] investigated the products of the co-hydrothermal treatment of food waste and yard waste, and found

that the solid products had higher energy density, higher mass density, and better mechanical properties. In this context, the co-hydrothermal treatment strategy of adding wood waste to food waste digestate has been proposed to improve the quality of the finished product.

Generally, to improve the efficiency and economic use of hydrothermal treatments, the products of different phases from hydrothermal liquefaction, such as bio-oil and hydrochar, need to be comprehensively improved. Catalysts are considered the most efficient tool to enhance product quality, especially that of bio-oil, under milder reaction conditions^[19]. Saber et al.^[20] improved the quality and yield of bio-oil by adding different kinds of catalysts, including nano-Ni/SiO₂, synthesized zeolite, and Na₂CO₃ during microalgae hydrothermal treatment. Imai et al.^[21] investigated the slurry obtained from the catalytic hydrothermal treatment of sawdust using K₂CO₃ as a catalyst, and found that the catalyst loading affected the element distribution and heating value of the slurry. Shah et al.^[22] studied the effects of an alkali catalyst (K₂CO₃) on product distribution from the hydrothermal liquefaction of sewage sludge, and found that the catalyst could improve the yield and quality of the bio-crude product. At present, there are many pieces of research that are focusing on the effects of catalysts on the liquid product of the hydrothermal reaction, while the effects on solid products have been neglected^[23,24]. In fact, exploring the effect of catalysts on solid product hydrochar is necessary to better exploit the application potential of hydrochar. Therefore, the catalytic co-hydrothermal strategy for food waste digestate and wood waste was proposed to investigate the effects of catalysts on solid products and in energy applications. This was done with the aim of contributing to the more efficient utilization of catalytic hydrothermal products.

In this study, hydrochar was prepared from food waste digestate and wood waste using a catalytic co-hydrothermal treatment based on alkali catalysts (K₂CO₃ and Na₂CO₃). The physicochemical properties of the hydrochar, including proximate analysis, element distribution, heating value, surface functional groups, and morphology, were explored. Based on these results, the gaseous products of pyrolysis and the combustion properties of the hydrochar were investigated using a thermogravimetric analyzer coupled with an infrared spectrophotometer and a mass spectrometer (TG-FTIR-MS) and a thermogravimetric analyzer coupled with a differential scanning calorimeter (TG-DSC), respectively. Furthermore, hydrochar combustion kinetics and thermodynamics were investigated. This study provides a basis for deconstructing the effect of catalysts on solid products in catalytic hydrothermal treatments, thereby improving the comprehensive utilization efficiency of this treatment.

2 Materials and methods

2.1 Materials and catalyst

Food waste digestate (FWD) and wood waste (WW) were collected from a local recycling department in Hong Kong. Because food waste digestate has a high ash content, which is not conducive to hydrothermal transformation and heat trans-

fer, it was washed with 1 mol·L⁻¹ HCl for deashing. Thereafter, the feedstock was pulverized to a size less than 30 mesh, and placed in an oven at 105 °C for 48 h. Potassium carbonate (K₂CO₃) and sodium carbonate (Na₂CO₃) were used as the alkali catalysts in this study.

2.2 Hydrochar preparation

A 500 mL Parr reactor was used for the hydrothermal experiments. For each experiment, 30 g of feedstock was mixed with 3 g of catalyst via wet impregnation using 150 mL of de-ionized water. The sealed reactor was heated to 250 °C at a rate of 10 °C·min⁻¹, which was maintained for 2 h. The speed of the stirrer was set at 200 r·min⁻¹, which was sustained to ensure adequate mixing. When the reaction was complete, the reactor was cooled to room temperature using circulating water. Hydrochar was obtained through filtration and placed in a 60 °C oven for 72 h for subsequent analysis. The hydrochar obtained using K₂CO₃ and Na₂CO₃ as catalysts were named HC-K and HC-Na, respectively.

2.3 Characterization of hydrochar

The ultimate analysis and heating value of the hydrochar were determined using an element analyzer and bomb calorimeter, respectively. The proximate analysis of the hydrochar was performed according to the guidelines of GB/T 28731–2012. The content of active alkali and alkaline earth metals (AAEMs) in the ash of the hydrochar was determined by inductively coupled plasma optical emission spectroscopy (ICP-OES).

The surface functional groups of the hydrochar were characterized using an infrared spectrophotometer in the range of 4000–400 cm⁻¹ wavenumbers. The crystalline structure of the hydrochar was analyzed using X-ray diffraction (XRD). Additionally, the surface morphology and surface elemental composition of the hydrochar were observed using scanning electron microscopy coupled with energy-dispersive X-ray spectroscopy (SEM-EDX). The chemical composition of the hydrochar surfaces was determined using X-ray photoelectron spectroscopy (XPS).

2.4 Thermal decomposition and combustion analysis

A thermogravimetric analyzer coupled with an infrared spectrophotometer and a mass spectrometer (TG-FTIR-MS) was used to analyze the thermal decomposition of the hydrochar. Approximately 10 mg of hydrochar was heated from room temperature to 900 °C, at a heating rate of 20 °C·min⁻¹, in a helium-filled atmosphere. The capillary line connecting the TG to the FTIR and the MS was kept at 250 °C, and the scan ranges for the FTIR and MS were 4000–400 cm⁻¹ and 44–300 (*m/z*), respectively.

The hydrochar combustion test was performed using a thermogravimetric analyzer coupled with a differential scanning calorimeter (TG-DSC), at a heating rate of 20 °C·min⁻¹, in air. Based on Eqs. (1) and (2), the comprehensive combustion index (CCI) and combustion stability index (CSI) were used to further evaluate the combustion performance of the hydrochar^[18].

$$CCI = \frac{DTG_{\max} \times DTG_{\text{mean}}}{T_i^2 T_b}, \quad (1)$$

$$CSI = 8.5875 \times 10^7 \times \frac{DTG_{\text{mean}}}{T_i T_{\text{max}}}, \quad (2)$$

where DTG_{max} and DTG_{mean} are the maximum mass loss rate and average mass loss rate ($\% \cdot \text{C}^{-1}$), respectively; and T_i , T_b , and T_{max} represent the ignition temperature, burnout temperature, and temperature with the maximum mass loss rate, respectively.

2.5 Kinetic and thermodynamic parameters

For kinetic analysis, the combustion characteristics of hydrochar at the heating rates of 10, 20, 30, and 40 $^{\circ}\text{C} \cdot \text{min}^{-1}$ were also obtained via thermogravimetric analysis. The activation energy (E_a), which represents the minimum energy for the reaction to occur, was calculated using the Flynn-Wall-Ozawa (FWO) and Kissinger-Akahira-Sunose (KAS) methods, as shown in Eq. (3) and Eq. (4), respectively^[25].

$$\ln \beta = \ln \left[\frac{A E_a}{R g(\alpha)} \right] - 5.331 - \frac{E_a}{RT}, \quad (3)$$

$$\ln \left(\frac{\beta}{T^2} \right) = \ln \left(\frac{AR}{E g(\alpha)} \right) - \frac{E_a}{RT}, \quad (4)$$

where β and E are the heating rate ($\text{K} \cdot \text{min}^{-1}$) and activation energy ($\text{kJ} \cdot \text{mol}^{-1}$), respectively; A and T represent the frequency factor (s^{-1}) and absolute temperature (K), respectively; and R is the universal gas constant ($8.314 \text{ J} \cdot \text{mol}^{-1} \cdot \text{K}^{-1}$). The value of α was calculated using Eq. (5) based on the thermogravimetric curve.

$$\alpha = \frac{m_0 - m_t}{m_0 - m_f}, \quad (5)$$

where m_0 , m_f , and m_t are the initial mass, the mass at the end of the reaction, and the mass of the sample at time t , respectively.

Based on Eqs. (3) and (4), the activation energy can be calculated from the slope of the plot of $\ln \beta$ or $\ln(\beta/T^2)$ versus $1/T$ at different heating rates.

In addition, thermodynamic parameters such as the enthalpy change (ΔH), Gibbs free energy change (ΔG), and entropy change (ΔS) were calculated using Eqs. (6)–(9)^[16, 26].

$$A = \frac{\beta E \exp \left(\frac{E}{RT_m} \right)}{RT_m^2}, \quad (6)$$

$$\Delta H = E - RT, \quad (7)$$

$$\Delta G = E + RT_m \ln \left(\frac{K_B T_m}{hA} \right), \quad (8)$$

$$\Delta S = \frac{\Delta H - \Delta G}{T_m}, \quad (9)$$

where K_B is the Boltzmann constant ($1.38064852 \times 10^{-23} \text{ J} \cdot \text{K}^{-1}$), T_m is peak temperature, and h is Planck's constant ($6.62607004 \times 10^{-34} \text{ J} \cdot \text{s}$).

3 Results and discussion

3.1 Evaluation of hydrochar properties

The physicochemical properties of the hydrochar obtained using different alkali catalysts were comprehensively analyzed. The proximate and ultimate analyses of the hydrochar are listed in Table 1. It was found that while HC-Na had a higher ash content, the fixed carbon content of the different hydrochars was similar. More carbon was present in HC-K, indicating that the sodium carbonate catalyst had a superior carbon fixation effect. In addition, the O/C ratio of HC-K was lower, indicating that HC-K was more stable. In contrast, HC-Na had a higher HHV, which was mainly attributed to its higher hydrogen content. The active alkali and alkaline earth metal contents of the hydrochar ash are shown in Table S1. It is clear that the hydrochar obtained with K_2CO_3 as the catalyst contained more potassium, whereas the hydrochar obtained with Na_2CO_3 as the catalyst contained more sodium. However, it cannot be ignored that calcium also played an important role in the ash, which was mainly derived from food waste digestate. There was more calcium in HC-Na, indicating that, as a catalyst, sodium carbonate could retain more calcium in the solid product during the hydrothermal process.

The infrared spectra of the hydrochar are depicted in Fig. 1a. HC-K and HC-Na had the same absorption peaks, mainly 3600–3200, 2928, 2860, 1766, 1636, 1535, 1444, and 1300–1100 cm^{-1} . Among them, the absorption band at 3600–3200 cm^{-1} was assigned to O–H, which was mainly attributed to the presence of H_2O and phenols in the hydrochar. The absorption peaks at 2928 cm^{-1} and 2860 cm^{-1} were related to the C–H vibrations, whereas those at 1766 cm^{-1} belonged to the C=O in aldehydes, ketones, and carboxylic acids^[27]. The absorption peaks at 1636 cm^{-1} and 1535 cm^{-1} corresponded to the aromatic skeleton, and the absorption peak at 1444 cm^{-1} was due to the presence of C–H deformation^[28]. Furthermore, the band at 1300–1100 cm^{-1} was attributed to the existence of R–OH^[29]. It is worth noting that HC-Na had stronger absorption peaks, indicating that the functional groups in HC-Na were more abundant. The XRD patterns of the hydrochars are shown in Fig. 1b. Both HC-K and HC-Na had some thin and prominent peaks representing KCl and NaCl, respectively, proving that a large amount of potassium and sodium was present in the hydrochar.

Fig. S1 shows SEM images of the surface morphology of

Table 1. The proximate analysis, ultimate analysis, and HHV of hydrochar (dry basis).

Samples	Proximate analysis $w_d(\%)$				Ultimate analysis $w_d(\%)$						HHV(MJ·kg ⁻¹)
	A	VM	FC ^a	VM/(VM+FC)	C	H	O ^a	N	O/C	H/C	
HC-K	13.17	58.48	28.35	0.67	58.63	6.50	17.17	4.53	0.22	1.33	23.71
HC-Na	14.37	57.58	28.05	0.67	55.75	7.29	17.59	5.00	0.24	1.57	26.85

[Note] ^a Calculated by difference.

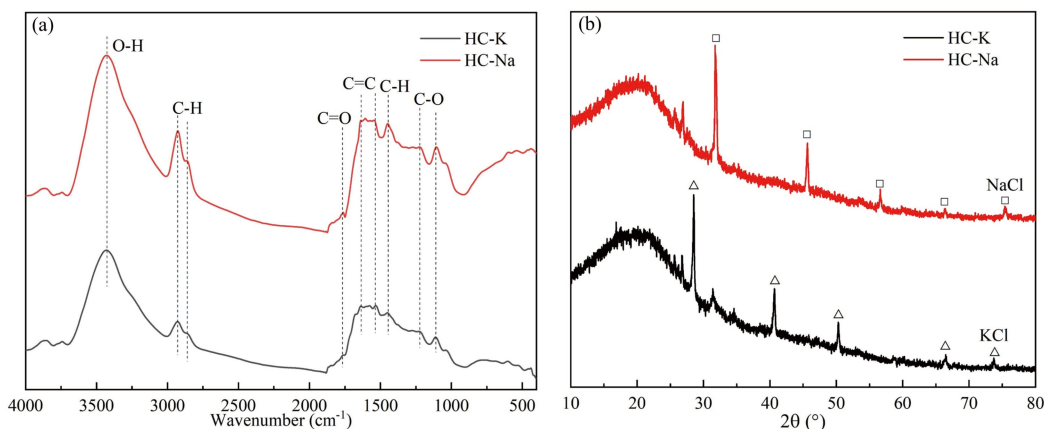


Fig. 1. The (a) infrared spectra and (b) XRD patterns of hydrochar.

the hydrochar. In these images, HC-K had more pores, whereas HC-Na had a rough surface, which may be due to its higher ash content. The EDX pattern also indicated the presence of potassium and sodium in HC-K and HC-Na, respectively. It was clear, as expected, that HC-K had more potassium and HC-Na had more sodium. In addition, chlorine was found, with its source mainly being from food waste digestate. Silicon and iron were also notable elements from the food waste digestate and wood waste. Meanwhile, other elements, such as aluminum, calcium, and magnesium, were also observed, which was consistent with the ICP results (Table S1).

The XPS spectra were obtained to further evaluate the surface functional groups of the hydrochar (Fig. S2). All spectra were calibrated based on C 1s. The C 1s spectrum was broken down into three distinctive peaks, which corresponded to C–C/C=C in the aromatic ring (284.8 eV), C–O (285.6 eV), and C=O (288.1 eV)^[30]. The ratio of C–C/C=C in the hydrochar was greater than 80%, revealing the presence of an abundant amount of aromatic rings. There were also more aromatic rings in HC-K, indicating that the potassium carbonate catalyst was more favorable for retaining the aromatic ring structure in the hydrochar. This is also consistent with the higher carbon content observed in HC-K. In addition, the O 1s spectrum consisted of four individual peaks, which corresponded to C=O (531.3 eV), C–O–C/–OH (532.5 eV), R'–O–R' (533.8 eV), and O–C=O/C–O (534.8 eV). Compared with HC-Na, the ratio of C–O–C/–OH components in HC-K was higher, which indicated that potassium carbonate

was more conducive to the formation of C–O–C/–OH in the hydrochar. In addition, HC-Na had a high proportion of C=O, indicating that sodium carbonate was more favorable for the formation of C=O. Nitrogen, as a compulsory component, directly affects the application of hydrochar owing to environmental protection. The nitrogen-containing functional groups (400 eV) in the hydrochar were separated into three common components (N-Q, N-5, and N-6). The ratio of N-5 in HC-K was higher than that of HC-Na with a small difference.

3.2 Analysis of the evolved gas

Pyrolysis is the first stage of carbonaceous feedstock combustion, and the gaseous products produced by pyrolysis form the basis for combustion. FTIR and MS were used to monitor the pyrolysis gas products of the hydrochar. Fig. 2 presents the infrared spectra of the gaseous products of hydrochar during pyrolysis as a function of temperature. Typical absorption peaks included mainly C–H (2930 cm⁻¹), CO (2180 cm⁻¹), C=O (1766 cm⁻¹), C=C (1636 cm⁻¹), and CO (1300–1100 cm⁻¹), and the substances containing these functional groups may be direct energy contributors during the combustion process. Naturally, the absorption peaks of H₂O (3600–3200 cm⁻¹) and CO₂ (2360 cm⁻¹) cannot be ignored. The infrared absorption peak of C–H was the most prominent, indicating that a large amount of hydrocarbons was generated during the pyrolysis of the hydrochar. Furthermore, with an increase in temperature, the infrared absorption peak gradually enhanced, and the most obvious infrared absorption peak was found

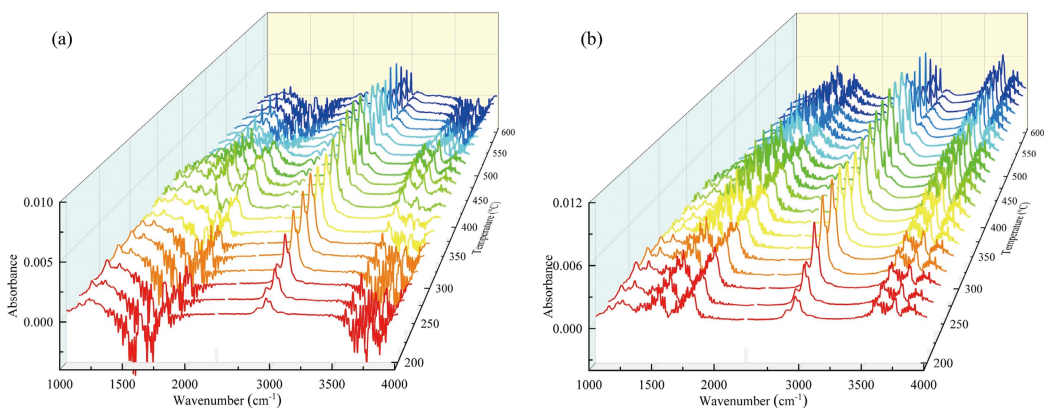


Fig. 2. FTIR spectrum of the gaseous products of hydrochar as a function of temperature for (a) HC-K and (b) HC-Na.

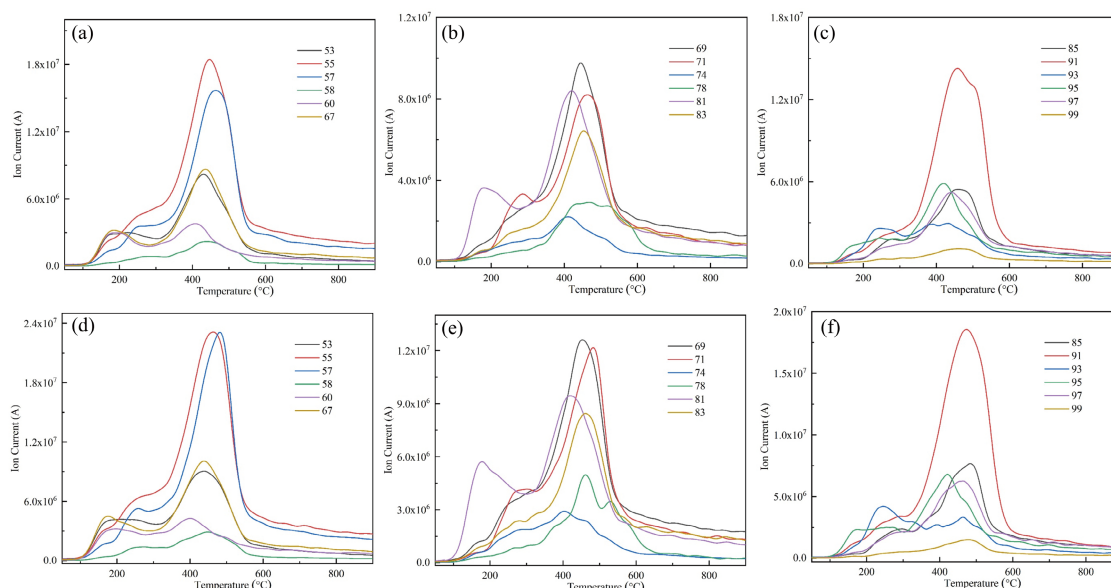


Fig. 3. Evolution curves of the main ionized fragments during hydrochar pyrolysis for HC-K (a–c) and HC-Na (d–f).

mainly in the temperature range of 300–500 °C. In addition, the infrared absorption peaks of the pyrolysis gas products of HC-Na were more attractive, indicating that the pyrolysis process of HC-Na was more intense, possibly because of the more obvious catalytic promotion effect of the AAEMs in HC-Na.

Although FTIR can detect pyrolysis gas products, such as hydrocarbons, phenols, aldehydes, and aromatics, it cannot identify the specific gas species. Therefore, MS analysis can be used as a supplementary method to more precisely define the species within pyrolysis gas products^[31]. The evolution curves of typical gas products as a function of temperature are shown in Fig. 3. The specific m/z and possible gaseous products are listed in Table S2^[32]. Typical ionized fragments (53, 55, 57, 58, 60, 67, 69, 71, 74, 78, 81, 83, 85, 91, 93, 95, 97, and 99) were selected because of their low intensities ($m/z > 100$)^[33].

During HC-K pyrolysis, the butene ($C_4H_7^+$) / propargyl alcohol ($C_3H_3O^+$) with an m/z of 55, butane ($C_4H_9^+$) with an m/z of 57, and toluene ($C_7H_7^+$) with an m/z of 91 had the most pronounced intensities, and their peak temperatures were 444, 469, and 457 °C, respectively. This indicates that a large amount of hydrocarbons was produced during the pyrolysis of HC-K. Pentane ($C_5H_{11}^+$) with an m/z of 71 and hexyne

($C_6H_9^+$) / 2-methylfuran ($C_5H_6O^+$) with an m/z of 81 also had relatively notable strength with prominent shoulders. This shows that these substances were produced during the co-hydrothermal process. The pyrolysis of HC-Na had the same prominent peaks and a similar temperature distribution as those of HC-K. It is worth noting that the strength of the ionized fragments of the pyrolysis products of HC-Na were significantly stronger than those of HC-K, which may be due to the active catalytic effects of sodium in the hydrochar. Simultaneously, the intensities of the ion fragments with m/z values of 71 and 81 increased relative to the m/z of 55. Thus, based on the information noted above, substantial hydrocarbon production was monitored during hydrochar pyrolysis, which facilitated the combustion process.

3.3 Combustion characteristics of hydrochar

Combustion performance analysis is the most direct method to assess the potential of hydrochar as a fuel. The combustion behavior of the hydrochar was revealed by TG-DSC analysis (Fig. 4). The combustion process can be divided into three stages: the release of moisture and volatiles, the main combustion stage, and the ash melting stage. The main combustion stage occurred between 190–680 °C. It was found that for HC-Na, both the TG-DTG and DSC curves shifted towards

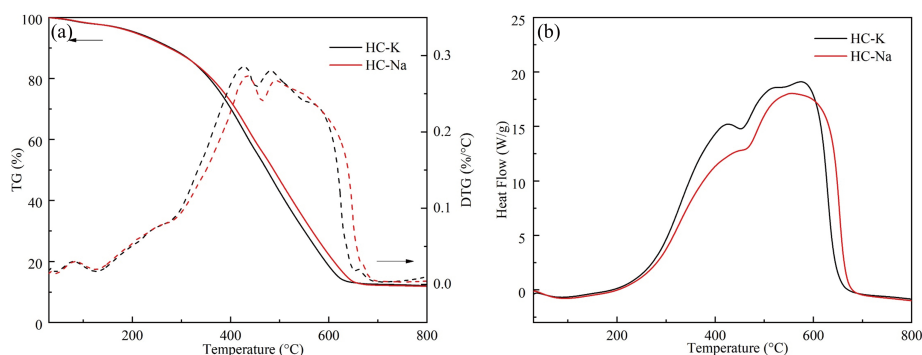


Fig. 4. Combustion performance (TG-DTG-DSC curves) of hydrochar.

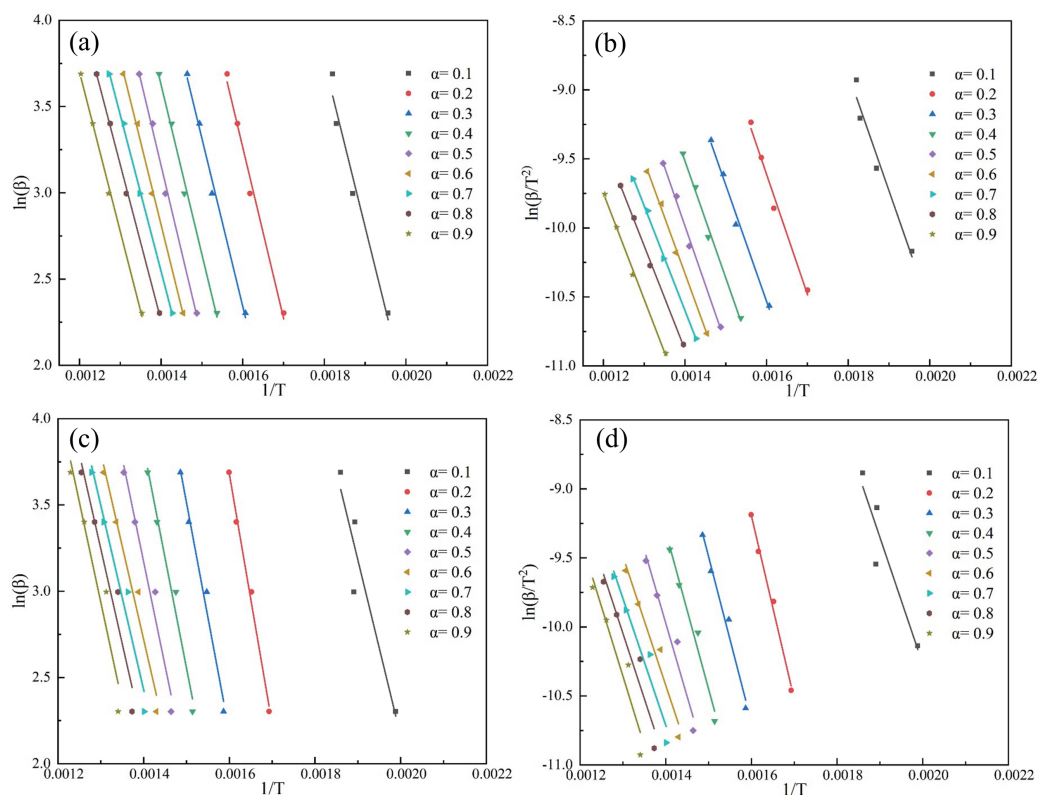


Fig. 5. The isoconversional plots of hydrochar at different conversion rates estimated using the KAS and FWO methods for HC-K (a–b) and HC-Na (c–d).

Table 2. Kinetics parameters for the combustion of hydrochar.

Samples		E_a with different conversion rates ($\text{kJ}\cdot\text{mol}^{-1}$)									Average
		0.1	0.2	0.3	0.4	0.5	0.6	0.7	0.8	0.9	
HC-K	FWO	79.36	82.34	80.88	81.70	82.64	79.66	75.33	75.11	76.89	79.32
	KAS	70.56	72.16	70.07	70.38	70.93	67.63	63.03	62.52	63.90	67.91
HC-Na	FWO	84.94	120.65	110.53	106.07	100.22	89.90	88.82	91.33	96.58	98.78
	KAS	76.32	110.55	99.71	94.69	88.41	77.74	76.40	78.67	83.63	87.35

the high-temperature region when compared with the HC-K curves. This may be due to the fact that HC-Na had a higher ash content. Correspondingly, HC-K released more heat in the low temperature range. The slope of the DTG curve was lower in the low-temperature region, which is generally considered to be the pyrolysis stage before the combustion of the hydrochar. Notably, there were two significant peaks at 428 °C and 479 °C in the combustion DTG curves of HC-K, and HC-Na exhibited the same pattern. Moreover, there was a setback near 450 °C in the DTG curve accompanied by an endotherm, which may be due to the eutectic reaction of the molten salt present in the hydrochar^[34].

Typical combustion parameters are listed in Table S3. The maximum mass loss rate for HC-K was $0.29\% \cdot \text{C}^{-1}$ at 428 °C, and the maximum mass loss rate for HC-Na was $0.27\% \cdot \text{C}^{-1}$ at 435 °C. HC-K had greater mass loss and average mass loss rates, but the ignition temperature, burnout temperature, and peak temperature were lower than those of HC-Na. Correspondingly, the comprehensive combustion and combustion stability indices of HC-K were higher, indicating that the combustion performance of HC-K was better.

3.4 Kinetic and thermodynamic analysis

Kinetic analysis of combustion is an important method used to evaluate combustion performance. The curves of $\ln(\beta)$ and $\ln(\beta/T^2)$ versus $1/T$ were plotted to obtain the activation energy based on the FWO and KAS methods, as shown in Fig. 5. The activation energy values at different conversion ratios (0.1–0.9) were calculated from the slope of the curve (Table 2). The correlation coefficient of the curve was greater than 0.9, indicating that the fitting is highly reliable.

During the combustion of HC-K, the activation energy values at different conversion ratios were within 75.11–82.64 $\text{kJ}\cdot\text{mol}^{-1}$ and 62.52–72.16 $\text{kJ}\cdot\text{mol}^{-1}$ using the FWO and KAS methods, respectively. The activation energy of HC-Na was within 84.94–120.65 $\text{kJ}\cdot\text{mol}^{-1}$ and 76.32–110.55 $\text{kJ}\cdot\text{mol}^{-1}$ using FWO and KAS methods, respectively. The combustion activation energy of HC-Na fluctuated more than that of HC-K, and the activation energy of HC-Na was higher than that of HC-K. This may be due to the fact that the acceleration effects of potassium during hydrochar combustion were stronger than those of sodium^[35, 36]. The activation energy var-

ied with the conversion rate, indicating that the combustion of hydrochar is a complex multistep reaction. In addition, HC-K had larger average activation energy values, estimated to be 98.78 kJ·mol⁻¹ and 87.35 kJ·mol⁻¹ using the FWO and KAS methods, respectively. This indicates that HC-Na needed to break through a larger energy barrier to begin combustion. Compared with the Ea of other feedstock such as rice husk (54.82 kJ·mol⁻¹)^[37], wheat straw (77.65 kJ·mol⁻¹)^[38], and corn straw (36.14 kJ·mol⁻¹)^[39], the hydrochar in this study had higher activation energy values.

The values of the thermodynamic parameters of hydrochar combustion were further calculated at the lowest heating rate (10 °C·min⁻¹) based on the FWO and KAS methods. At low heating rates, the thermal decomposition process was more precise; the results for which are presented in Table 3. HC-Na had a larger pre-exponential factor (*A*) (estimated to be 6.32×10³ s⁻¹ with the FWO method and 8.18×10³ s⁻¹ with the KAS method), indicating higher molecular collisions to be transferred^[26]. The enthalpy change (ΔH) refers to the total energy change within the system. It is clear that the trends of enthalpy change and activation energy were consistent, and HC-K had a higher value (73.55 kJ·mol⁻¹ as estimated using the

FWO method and 62.14 kJ·mol⁻¹ estimated using the KAS method). Comparing the ΔH with the Ea values of hydrochar, there was a small potential energy barrier (approximately 6 kJ·mol⁻¹), which demonstrates the feasibility of the combustion reaction. The smaller the difference of ΔH to Ea values, the more likely the thermal conversions of hydrochar are to occur^[40]. The Gibbs free energy change (ΔG) represents the total energy increase in a system^[25]. Although HC-K had a smaller ΔG (estimated to be 207.79 kJ·mol⁻¹ using the FWO method and 208.69 kJ·mol⁻¹ using the KAS method), it was not very different from that of HC-Na. This indicates that the difference in energy production between HC-K and HC-Na was small. The entropy change (ΔS) represents the degree of disorder within a system^[16]. It is worth noting that all the values of entropy change during the hydrochar combustion were negative. The entropy changes in HC-K were estimated to be -193.44 J·mol⁻¹·K⁻¹ and -211.17 J·mol⁻¹·K⁻¹ using the FWO and KAS methods, respectively, while those of HC-Na were -168.59 J·mol⁻¹·K⁻¹ and -185.59 J·mol⁻¹·K⁻¹, respectively. Negative ΔS values indicate a lower degree of disorder among the products^[41].

Table 3. Thermodynamic parameters calculated using the FWO and KAS methods at a heating rate of 10 °C·min⁻¹.

Samples		<i>A</i> (s ⁻¹)	ΔH (kJ·mol ⁻¹)	ΔG (kJ·mol ⁻¹)	ΔS (J·mol ⁻¹ ·K ⁻¹)
HC-K	FWO	3.09×10 ³	73.55	207.79	-193.44
	KAS	3.66×10 ³	62.14	208.69	-211.17
HC-Na	FWO	6.32×10 ³	92.83	213.43	-168.59
	KAS	8.18×10 ³	81.40	214.16	-185.59

4 Conclusions

Carbon-rich hydrochar with a high heating value (up to 26.85 MJ·kg⁻¹) was prepared from food waste digestate and wood waste using catalytic co-hydrothermal treatment. The resulting hydrochar possessed abundant functional groups and the ability to retain alkali metal elements. The hydrochar pyrolysis gas contained a notable amount of hydrocarbons, and the intensity of HC-Na was greater. HC-K demonstrated a higher comprehensive combustion index and lower combustion activation energy values (79.32 kJ·mol⁻¹ and 67.91 kJ·mol⁻¹ estimated using the FWO and KAS methods, respectively). The thermodynamic parameters confirmed the superior combustion reactivity of hydrochar. This study demonstrated that food waste digestate can be regarded as a potential energy-generating raw material through a catalytic co-hydrothermal process. In so doing, its comprehensive and efficient utilization may be realized. It is worth noting that the complexity of the feedstock may limit the catalytic hydrothermal treatment effect. In future works, the types of solid waste and larger scale need to be further explored.

Supporting information

The supporting information for this article can be found online at <https://doi.org/10.52396/JUSTC-2022-0049>. It includes two figures and three tables.

Acknowledgements

The authors acknowledge the extended help from the Instru-

ments' Center for Physical Science of University of Science and Technology of China. This work was supported by the Fundamental Research Funds for the Central Universities (WK2090000037), and the funding of the Hong Kong Scholars Program (XJ2020022).

Conflict of interest

The authors declare that they have no conflict of interest.

Biographies

Xiefei Zhu is currently a postdoctoral fellow supported by the Hong Kong Scholars Program. He received his Ph.D. degree from the University of Science and Technology of China in 2020. He is dedicated to the high-value utilization of organic solid waste such as biomass, converting organic solid waste into fuel and added-value chemicals. He also focuses on the application of biochar in adsorption and CO₂ reduction, developing various types of efficient carbon-based adsorbents.

References

- [1] Yang Q, Zhou H, Bartocci P, et al. Prospective contributions of biomass pyrolysis to China's 2050 carbon reduction and renewable energy goals. *Nature Communication*, 2021, 12 (1): 1698.
- [2] Soltani S, Khanian N, Shean Yaw Choong T, et al. Microwave-assisted hydrothermal synthesis of sulfonated TiO₂-GO core-shell solid spheres as heterogeneous esterification mesoporous catalyst for biodiesel production. *Energy Conversion and Management*, 2021, 238: 114165.
- [3] Zhao S, Li J, Chen C, et al. Interpretable machine learning for

- predicting and evaluating hydrogen production via supercritical water gasification of biomass. *Journal of Cleaner Production*, **2021**, *316*: 128244.
- [4] Zeng J, Xiao R, Yuan J. High-quality syngas production from biomass driven by chemical looping on a PY-GA coupled reactor. *Energy*, **2021**, *214*: 118846.
- [5] Akyürek Z. Sustainable valorization of animal manure and recycled polyester: Co-pyrolysis synergy. *Sustainability*, **2019**, *11* (8): 2280.
- [6] Aierzhati A, Watson J, Si B, et al. Development of a mobile, pilot scale hydrothermal liquefaction reactor: Food waste conversion product analysis and techno-economic assessment. *Energy Conversion and Management: X*, **2021**, *10*: 100076.
- [7] Lu J, Xu S. Post-treatment of food waste digestate towards land application: A review. *Journal of Cleaner Production*, **2021**, *303*: 127033.
- [8] Manu M K, Li D, Liwen L, et al. A review on nitrogen dynamics and mitigation strategies of food waste digestate composting. *Bioresource Technology*, **2021**, *334*: 125032.
- [9] Xu J, Dong X, Wang Y. Hydrothermal liquefaction of macroalgae over various solids, basic or acidic oxides and metal salt catalyst: Products distribution and characterization. *Industrial Crops and Products*, **2020**, *151*: 112458.
- [10] Zhang C, Shao M, Wu H, et al. Mechanism insights into hydrothermal dewatering of food waste digestate for products valorization. *Science of The Total Environment*, **2022**, *804*: 150145.
- [11] Xie X, Peng C, Song X, et al. Pyrolysis kinetics of the hydrothermal carbons derived from microwave-assisted hydrothermal carbonization of food waste digestate. *Energy*, **2022**, *245*: 123269.
- [12] Zhang C, Shao M, Wu H, et al. Management and valorization of digestate from food waste via hydrothermal. *Resources, Conservation and Recycling*, **2021**, *171*: 105639.
- [13] Dutta S, He M, Xiong X, et al. Sustainable management and recycling of food waste anaerobic digestate: A review. *Bioresource Technology*, **2021**, *341*: 125915.
- [14] Zhang X, Zhang L, Li A. Co-hydrothermal carbonization of lignocellulosic biomass and waste polyvinyl chloride for high-quality solid fuel production: Hydrochar properties and its combustion and pyrolysis behaviors. *Bioresource Technology*, **2019**, *294*: 122113.
- [15] Xu D, Wang Y, Lin G, et al. Co-hydrothermal liquefaction of microalgae and sewage sludge in subcritical water: Ash effects on bio-oil production. *Renewable Energy*, **2019**, *138*: 1143–1151.
- [16] Lang Q, Zhang B, Liu Z, et al. Co-hydrothermal carbonization of corn stalk and swine manure: Combustion behavior of hydrochar by thermogravimetric analysis. *Bioresource Technology*, **2019**, *271*: 75–83.
- [17] Lu X, Ma X, Chen X. Co-hydrothermal carbonization of sewage sludge and lignocellulosic biomass: Fuel properties and heavy metal transformation behaviour of hydrochars. *Energy*, **2021**, *221*: 119896.
- [18] Sharma H B, Dubey B K. Co-hydrothermal carbonization of food waste with yard waste for solid biofuel production: Hydrochar characterization and its pelletization. *Waste Management*, **2020**, *118*: 521–533.
- [19] Koley S, Khadase M S, Mathimani T, et al. Catalytic and non-catalytic hydrothermal processing of *Scenedesmus obliquus* biomass for bio-crude production: A sustainable energy perspective. *Energy Conversion and Management*, **2018**, *163*: 111–121.
- [20] Saber M, Golzary A, Hosseinpour M, et al. Catalytic hydrothermal liquefaction of microalgae using nanocatalyst. *Applied Energy*, **2016**, *183*: 566–576.
- [21] Imai A, Hardi F, Lundqvist P, et al. Alkali-catalyzed hydrothermal treatment of sawdust for production of a potential feedstock for catalytic gasification. *Applied Energy*, **2018**, *231*: 594–599.
- [22] Shah A A, Toor S S, Conti F, et al. Hydrothermal liquefaction of high ash containing sewage sludge at sub and supercritical conditions. *Biomass and Bioenergy*, **2020**, *135*: 105504.
- [23] Xu D, Lin G, Guo S, et al. Catalytic hydrothermal liquefaction of algae and upgrading of biocrude: A critical review. *Renewable and Sustainable Energy Reviews*, **2018**, *97*: 103–118.
- [24] Nagappan S, Bhosale R R, Nguyen D D, et al. Catalytic hydrothermal liquefaction of biomass into bio-oils and other value-added products: A review. *Fuel*, **2021**, *285*: 119053.
- [25] Chong C T, Mong G R, Ng J-H, et al. Pyrolysis characteristics and kinetic studies of horse manure using thermogravimetric analysis. *Energy Conversion and Management*, **2019**, *180*: 1260–1267.
- [26] Boubacar Laougé Z, Merdun H. Kinetic analysis of Pearl Millet (*Penisetum glaucum* (L) R. Br.) under pyrolysis and combustion to investigate its bioenergy potential. *Fuel*, **2020**, *267*: 117172.
- [27] Zhu X, Li K, Zhang L, et al. Synergistic effects on thermochemical behaviors of co-pyrolysis between bio-oil distillation residue and bituminous coal. *Energy Conversion and Management*, **2017**, *151*: 209–215.
- [28] Zhang L, Li K, Zhu X. Study on two-step pyrolysis of soybean stalk by TG-FTIR and Py-GC/MS. *Journal of Analytical and Applied Pyrolysis*, **2017**, *127*: 91–98.
- [29] Zhu X, Luo Z, Diao R, et al. Combining torrefaction pretreatment and co-pyrolysis to upgrade biochar derived from bio-oil distillation residue and walnut shell. *Energy Conversion and Management*, **2019**, *199*: 111970.
- [30] Zhu X, Luo Z, Guo W, et al. Reutilization of biomass pyrolysis waste: Tailoring dual-doped biochar from refining residue of bio-oil through one-step self-assembly. *Journal of Cleaner Production*, **2022**, *343*: 131046.
- [31] Sun C, Li C, Tan H, et al. Synergistic effects of wood fiber and polylactic acid during co-pyrolysis using TG-FTIR-MS and Py-GC/MS. *Energy Conversion and Management*, **2019**, *202*: 112212.
- [32] Kai X, Li R, Yang T, et al. Study on the co-pyrolysis of rice straw and high density polyethylene blends using TG-FTIR-MS. *Energy Conversion and Management*, **2017**, *146*: 20–33.
- [33] Kai X, Yang T, Shen S, et al. TG-FTIR-MS study of synergistic effects during co-pyrolysis of corn stalk and high-density polyethylene (HDPE). *Energy Conversion and Management*, **2019**, *181*: 202–213.
- [34] Zeng K, Yang X, Xie Y, et al. Molten salt pyrolysis of biomass: The evaluation of molten salt. *Fuel*, **2021**, *302*: 121103.
- [35] Safar M, Lin B-J, Chen W-H, et al. Catalytic effects of potassium on biomass pyrolysis, combustion and torrefaction. *Applied Energy*, **2019**, *235*: 346–355.
- [36] Liu Y, Wang Z, Wan K, et al. In situ measurements of the release characteristics and catalytic effects of different chemical forms of sodium during combustion of Zhundong coal. *Energy & Fuels*, **2018**, *32* (6): 6595–6602.
- [37] Wang T, Fu T, Chen K, et al. Co-combustion behavior of dyeing sludge and rice husk by using TG-MS: Thermal conversion, gas evolution, and kinetic analyses. *Bioresource Technology*, **2020**, *311*: 123527.
- [38] Ma Q, Han L, Huang G. Effect of water-washing of wheat straw and hydrothermal temperature on its hydrochar evolution and combustion properties. *Bioresource Technology*, **2018**, *269*: 96–103.
- [39] Guo S, Tan J, Yang Z, et al. Mixed-combustion characteristics and reaction kinetics of municipal sludge and corn straw in micro-fluidized bed. *Energies*, **2022**, *15* (7): 2637.
- [40] Loy A C M, Gan D K W, Yusup S, et al. Thermogravimetric kinetic modelling of in-situ catalytic pyrolytic conversion of rice husk to bioenergy using rice hull ash catalyst. *Bioresource Technology*, **2018**, *261*: 213–222.
- [41] Ahmad M S, Mehmood M A, Al Ayed O S, et al. Kinetic analyses and pyrolytic behavior of Para grass (*Urochloa mutica*) for its bioenergy potential. *Bioresource Technology*, **2017**, *224*: 708–713.